Article

Effective Adsorption of Chlorinated Polyfluoroalkyl Ether Sulfonates from Wastewater by Nano-Activated Carbon: Performance and Mechanisms

Hao Yi [1,2], Xiaolin Chen [3], Zewei Liu [4], Hongxia Xi [3], Zecong Ding [2], Kai Cui [1,2,*] and Yongyou Hu [1,*]

[1] School of Environment and Energy, South China University of Technology, Guangzhou 510006, China
[2] South China Environmental Forensic Center, South China Institute of Environmental Science, Ministry of Ecology and Environment (MEE), Guangzhou 510655, China
[3] School of Chemistry and Chemical Engineering, South China University of Technology, Guangzhou 510006, China
[4] School of Environmental and Chemical Engineering, Foshan University, Foshan 528225, China
* Correspondence: cuikai@scies.org (K.C.); ppyyhu@scut.edu.cn (Y.H.)

Abstract: Chlorinated polyfluoroalkyl ether sulfonates (F-53B) were often used as mist suppressants in the chrome plating industry, resulting in the large discharge of F-53B-containing electroplating wastewater into the aquatic environment. Due to the high toxicity of F-53B, increasing attention has been paid to its efficient removal from wastewater. In this study, three nano-activated carbons were successfully prepared from coconut shell carbons by a simple one-step KOH activation method. The nitrogen adsorption/desorption experiments showed that the synthesized coconut shell activated carbons possessed a well-developed nano-pore structure, which was favorable for the adsorption of F-53B. The results suggested that the adsorption of F-53B on the coconut shell activated carbons followed pseudo-second-order kinetics and was better fitted in the Langmuir isotherm, indicating that the adsorption of F-53B was mainly controlled by chemical adsorption and was mainly monolayer adsorption. Theoretical calculation results revealed that the faster adsorption rate of F-53B on CSAC_800 than on CSAC_600 and CSAC_700 could be contributed to the lower adsorption energy of F-53B on CSAC_800 and the higher self-diffusion coefficients of F-53B in CSAC_800. The higher adsorption capacity of CSAC_800 (q_m = 537.6 mg·g^{-1}) for F-53B than that of CSAC_600 (q_m = 396.83 mg·g^{-1}) and CSAC_700 (q_m = 476.19 mg·g^{-1}) could be attributed to the higher specific surface area and larger number of adsorption sites of CSAC_800. The results of this study demonstrate that coconut shell activated carbons with a well-developed nano-pore structure are an effective adsorbent for F-53B removal and have a good application prospect.

Keywords: coconut shell activated carbon; nano-pore structure; chlorinated polyfluoroalkyl ether sulfonates; grand canonical Monte Carlo; adsorption energy

1. Introduction

Perfluorooctane sulfonate (PFOS), a representative long-chain (C = 8) perfluoroalkyl compound, was widely used in industrial production fields such as surface coatings, fire-fighting foams, and metal plating [1,2]. However, due to the persistence, bioaccumulation, and toxicity of PFOS in the environment [3], PFOS was listed as one of the persistent organic pollutants of the Stockholm Convention in 2009, with strict restrictions on its production and utilization in many countries [4]. Hence, the industrial demand for related alternatives to PFOS has increased [5]. As an important alternative to PFOS, chlorinated polyfluoroalkyl ether sulfonates (F-53B) have occupied a large market in the electroplating industry due to their low production cost and simple preparation process and have gradually replaced PFOS as a mist suppressant in the chrome plating industry [6].

Due to the widespread use of F-53B in the chrome plating industry, a large amount of F-53B-containing wastewater was discharged into the aquatic environment, and its

environmental risks and health hazards have received increasing concern [7,8]. At the same time, toxicological studies have shown that F-53B has various toxic effects, such as hepatotoxicity, reproductive toxicity, and developmental toxicity, posing a great threat to human health [9]. In view of the wide distribution and potential harm of F-53B, it is necessary to take effective measures to reduce its threat.

At present, the main methods for removing perfluoroalkyl compounds include adsorption [10–12], biodegradation [13,14], photocatalysis [15–17], and electrocatalysis [18–20]. Among them, adsorption is widely used because of its advantages of easy operation, low cost, and low energy consumption [21]. Clay [22], anion exchange resin [23], activated carbon [24], and metal-organic skeleton materials [25] were usually used as adsorbents. Among them, activated carbon has become an important adsorbent for removing perfluoroalkyl compounds due to its low cost, renewable nature, high porosity, and large specific surface area [26]. Since F-53B is a substitute for PFOS and has a similar chemical structure and properties to PFOS, it is speculated that activated carbon can also efficiently adsorb F-53B.

In this study, coconut shell-activated carbons with a well-developed nano-pore structure were prepared by one-step activation of potassium hydroxide (KOH) for efficient adsorption of F-53B-form wastewater. The nitrogen (N_2) adsorption/desorption experiments were carried out to investigate the specific surface area and pore structure of the synthesized activated carbon. Adsorption kinetics and adsorption equilibrium experiments were carried out to investigate the adsorption rate and capacity of F-53B by the synthesized activated carbon. Finally, grand canonical Monte Carlo (GCMC) simulation combined with molecular dynamics (MD) was used to study the adsorption mechanism of F-53B by the synthesized activated carbon. This study offered a comprehensive understanding of the adsorption performance and mechanisms of F-53B by coconut shell activated carbons, so as to explore the potential of its industrial application.

2. Materials and Methods

2.1. Materials

F-53B (Figure 1) was purchased from Jianglai Biotechnology Co., Ltd. (Shanghai, China). Coconut shell carbon was purchased from Bailingwei Technology Co., Ltd. (Beijing, China). Potassium hydroxide (KOH) and hydrochloric acid (HCl) were purchased from Guanghua Sci-Tech Co., Ltd. (Guangzhou, China). High-purity nitrogen (99.999%) was purchased from Guangzhou Yingsheng Gas Co., Ltd. (Guangzhou, China). All chemicals used in this study were analytical grade or better, and all solutions were prepared with deionized (DI) water.
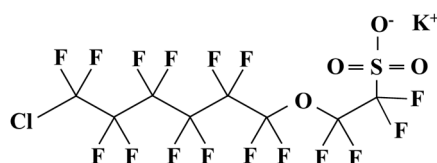

Figure 1. Scheme of the molecular structure of F-53B.

2.2. Preparation of Coconut Shell Active Carbon

The commercial coconut shell carbon was crushed with a grinder, and 0.5 g of coconut shell carbon particles were mixed with 2 g of KOH, and they were ground into powder. Then, the powder was placed in a tube furnace, which was raised to a certain temperature at a heating rate of 5 °C/min in an N_2 atmosphere for 2 h. Finally, the products were washed to neutrality with 1 mol/L HCl solution and DI water and dried at 105 °C for 12 h. To investigate the impacts of activation temperature on the pore structure of activated carbons, three activation temperatures were studied in this work. When the activation temperature is too high ($\geq$900 °C), KOH is too corrosive, and it is easy to corrode the porcelain boat and introduce impurities, which eventually leads to a significant decline in sample purity.

Therefore, the active temperature was set to 600, 700, and 800 °C in this study, and the products were denoted as CSAC_600, CSAC_700, and CSAC_800, respectively.

2.3. Characterization of Coconut Shell Active Carbon

The specific surface area of coconut shell active carbons was measured by BET N_2 adsorption analysis using a Micromeritics ASAP2460 apparatus (Micromeritics ASAP2460, Atlanta, GA, USA). The BET surface area was calculated from the isotherms using the Brunauer–Emmett–Teller (BET) model. The pore size distribution and pore volume were derived from the Barrett-Joyner-Halenda (BJH) model. Elemental analysis of coconut shell active carbons was performed on an elemental analyzer (Flash 2000, Thermo Fisher Scientific, Bremen, Germany). The samples were dried at 105 °C for 1 h and then placed in the analyzer and mixed with vanadium pentoxide (V_2O_5) to enhance combustion. The prepared sample was then burned for 600 s at a temperature of 960 °C using a standard methionine for hydrogen determination and 2,5-(bis (5-tert-butyl-2-benz-axazol-2-yl) thiophene for oxygen determination.

2.4. Adsorption Experiments

All batch adsorption experiments were performed in 100 mL conical flasks containing 50 mL of F-53B stock solution, and the concentration of coconut shell active carbon was 0.2 g/L. The pH of the reaction was controlled at 7.0 ± 0.3. All conical flasks were shaken in a thermostatic shaker (180 ± 5 rpm) at 25 ± 1 °C. Adsorption kinetics were performed in a 50 mg/L F-53B solution, and the suspension samples were taken after reactions for 0.5, 1, 1.5, 2, 4, 6, 8, 10, 15, 20, 60, 180, 420, 960, and 1440 min. Adsorption isotherms were performed at initial F-53B concentrations of 5–150 mg/L, and the reaction time was set to 24 h to ensure the adsorption equilibrium was reached. After reactions, the suspension samples were filtered through 0.22 μm membrane filters to remove coconut shell active carbon, and the 0.22 μm membrane filters had negligible impacts on the determination of F-53B [23]. The concentration of F-53B in the filtrates was determined with high-performance liquid chromatography (Dionex UltiMate 3000, Thermo Fisher Scientific, Waltham, MA, USA) coupled with a triple quadrupole mass spectrometer (TSQ Vantage, Thermo Fisher Scientific, Waltham, MA, USA) (HPLC-MS/MS). A HPH-C18 analytical column was used in this study. Mobile phases consisted of 2 mM ammonium acetate (A) and acetonitrile (B). Gradient conditions were used at a 0.3 mL/min flow rate, and 5 μL of the sample was injected, starting with 80% A and 20% B. The initial conditions were held for 1.8 min and then decreased to 10% A at 2 min, held till 4 min, returned to the initial condition at 4.2 min, and finally held constant until 6 min. The temperature of the column oven was kept constant at 40 °C.

2.5. Analysis of Adsorption Kinetics and Isotherms

The adsorption capacity and the adsorption efficiency of coconut shell active carbon for F-53B were calculated by the following equations:

$$q_t = \frac{(C_0 - C_t) \times V}{m} \tag{1}$$

$$q_e = \frac{(C_0 - C_e) \times V}{m} \tag{2}$$

$$\eta = \frac{(C_0 - C_e)}{C_0} \times 100\% \tag{3}$$

where q_t and q_e are the capacities at time (t) and at equilibrium, respectively, and η represents the adsorption efficiency. In addition, C_0, C_t, and C_e (mg/L) are the concentrations of F-53B at the adsorption times (min) at zero, t, and equilibrium. V (L) is the solution volume, and m (g) is the mass of coconut shell active carbon used.

The adsorption kinetic data were analyzed by pseudo-first-order and pseudo-second-order kinetic models using the following equations:

Pseudo-first-order kinetic model:

$$q_t = q_e \left(1 - e^{-k_1 t}\right) \tag{4}$$

Pseudo-second-order kinetic model:

$$\frac{t}{q_t} = \frac{1}{q_e^2 k_2} + \frac{t}{q_e} \tag{5}$$

where k_1 (min^{-1}) and k_2 (min^{-1}) are the pseudo-first-order rate constant and pseudo-second-order rate constant, respectively.

The adsorption isotherm data were analyzed using the Langmuir and Freundlich isotherm models as follows:

Langmuir isotherm model:

$$q_e = \frac{K_L q_m C_e}{1 + K_L C_e} \tag{6}$$

Freundlich isotherm model:

$$q_e = K_F C_e^{1/n} \tag{7}$$

where K_L (L/mg) is the Langmuir constant; q_m (mg/g) is the maximum adsorption capacity; K_F and n are the Freundlich constants.

2.6. Theoretical Calculations

In this study, the effects of different pore sizes on the adsorption of F-53B by coconut shell activated carbon were investigated using a slit pore model. The model of coconut shell activated carbon was modified from the original graphite carbon model ($11 \times 11 \times 1$ supercell) according to the atomic ratio obtained from the elemental analysis results, in which several common oxygen-containing groups were considered for the corresponding oxygen elements, such as heteroepoxy atoms, hydroxyl groups, and carboxyl groups. It is inferred that the coconut shell activated carbon exhibits varying degrees of defects because the oxygen content of the three materials is high.

In addition, GCMC simulation combined with MD was used to study the adsorption mechanism of F-53B by coconut shell activated carbon. All calculations were carried out in Materials Studio 7.0. The model of coconut shell activated carbon was optimized by the Forcite module. In the optimization, the convergence standards of energy, force, and displacement were 1×10^{-4} kcal/mol/Å, 1×10^{-5} kcal/mol, and 5×10^{-5} Å, respectively. Based on the optimized model, the fixed loading task of the Sorption module is used to calculate the adsorption interaction energy curve of a single F-53B molecule in coconut shell activated carbon models with different pore sizes. The van der Waals force involved in the adsorption process is described by Lennard-Jones 12-6 [27], and its parameters are derived from the UFF force field [28]. The electrostatic force is calculated using the Ewald method. The charge of the skeleton atom is calculated by the QEq method, while the atomic partition charge of the F-53B molecule is calculated by the ESP method. Before charge calculation, F-53B molecules should be optimized with the DMOL3 module in fine quality. The basis set is GGA/PBE, and the dispersion force is corrected by Grimme. In order to accurately simulate the adsorption behavior of F-53B molecules in the skeleton, the motion of F-53B is described by different moving types, including insertion, deletion, translation, regeneration, and rotation. The total number of steps for both initialization and balancing is 2×10^5, and the simulated cut-off radius is 12.0 Å.

The radial distribution function (RDF) curve is often used to qualitatively analyze the strength of interactions between different sites in the adsorbent molecule and different sites in the adsorbate molecule [29–31]. In this study, the RDF curves between different sites in a single F-53B molecule and different adsorption sites in the coconut shell activated

carbon skeleton were calculated using Materials Studio 7.0. The Locate task of the Sorption module is used to insert an F-53B molecule into the coconut shell activated carbon model. The Dynamic task in the Forcite module is used to conduct a dynamic simulation of the coconut shell activated carbon model that adsorbs a single F-53B molecule. The NVT ensemble is used to achieve the system's equilibrium, and the temperature is adjusted by the Nose–Hoover hot bath method, and then the NVE ensemble is used to calculate the equilibrium system further. The step size of the two calculations is 1 fs, and the total time is 10 ns. Based on the calculation results, the self-diffusion coefficient of a single F-53B molecule in different coconut shell activated carbon models was also calculated (Equation (8)).

$$D_S = \frac{1}{6} \lim_{t \to \infty} \frac{d}{d_t} (\frac{1}{N} \sum_{i=1}^{N} [r_i(t) - r_i(t_0)]^2) \tag{8}$$

where N is the number of F-53B molecules, and $r_i(t)$ is the location of the F-53B molecule i at time t.

3. Results and Discussion

3.1. Characterization of Coconut Shell Activated Carbon

The adsorption capacity of adsorbents is closely related to the specific surface area and pore structure of the adsorbents [32]. In order to investigate the effect of different activation temperatures on the pore structure of coconut shell-activated carbon, N_2 adsorption and desorption experiments were carried out on the prepared coconut shell-based activated carbons at 77 K. As shown in Figure 2a, the N_2 adsorption-desorption isotherms of three coconut shell activated carbons are all type I, and when the relative pressure P/P_0 is less than 0.1, the adsorption amount of N_2 increases rapidly, indicating that three coconut shell activated carbons all have a rich microporous structure. The P and P_0 represent the actual pressure and saturated vapor pressure of N_2 at the measured temperature, respectively. The relative pressure P/P_0 can be increased by increasing the input of N_2, which enhances the adsorption of N_2 on adsorbents. According to the International Union of Pure and Applied Chemistry (IUPAC) classification, there are six types of N_2 adsorption-desorption isotherm curves. The N_2 adsorption-desorption isotherms of activated carbons usually exhibit type I, suggesting that they are microporous [33,34]. The results of pore size distribution further confirmed that the three kinds of coconut shell activated carbons were mainly micropores, which were mainly distributed at 0.8 nm, 1.2 nm, and 1.5 nm, and had a small number of mesoporous pores (>2 nm) (Figure 2b). According to the parameters of pore structure (Table 1), the specific surface area and total pore volume of coconut shell activated carbon increase with the increase of activation temperature, which can be attributed to the fact that the increase of activation temperature promotes the corrosion of KOH to the coconut shell carbon and promotes the formation of nanopores. During the corrosion process, potassium-containing compounds such as K_2CO_3, K_2O, and K were formed. When the activation temperature further reaches the boiling point of metal potassium (762 °C), the potassium vapor escapes and diffuses into the carbon layer, resulting in an enlarged carbon lattice and richer nanopore structure.

Table 1. Specific surface area and total pore volume of three coconut shell-activated carbons.

Samples	$S_{BET}/(m^2/g^{-1})$	$V_{tol}/(cm^3/g)$
CSAC_600	1117	0.49
CSAC-700	1355	0.56
CSAC-800	1509	0.71

The elemental analysis results of coconut shell activated carbons are shown in Table 2. As the activation temperature increased from 600 °C to 800 °C, the carbon content of the coconut shell activated carbon increased, indicating that the activation temperature increased the carbonization degree of the coconut shell carbon [35]. The decrease in the

content of hydrogen and oxygen elements may be due to the escape of gases (such as water vapor (H_2O) and potassium oxide (K_2O) gas) produced in the process of high-temperature pyrolysis [36,37]. The escape of gases creased a complex porous network and increased the specific surface area of coconut shell activated carbons (Figure 2 and Table 1).
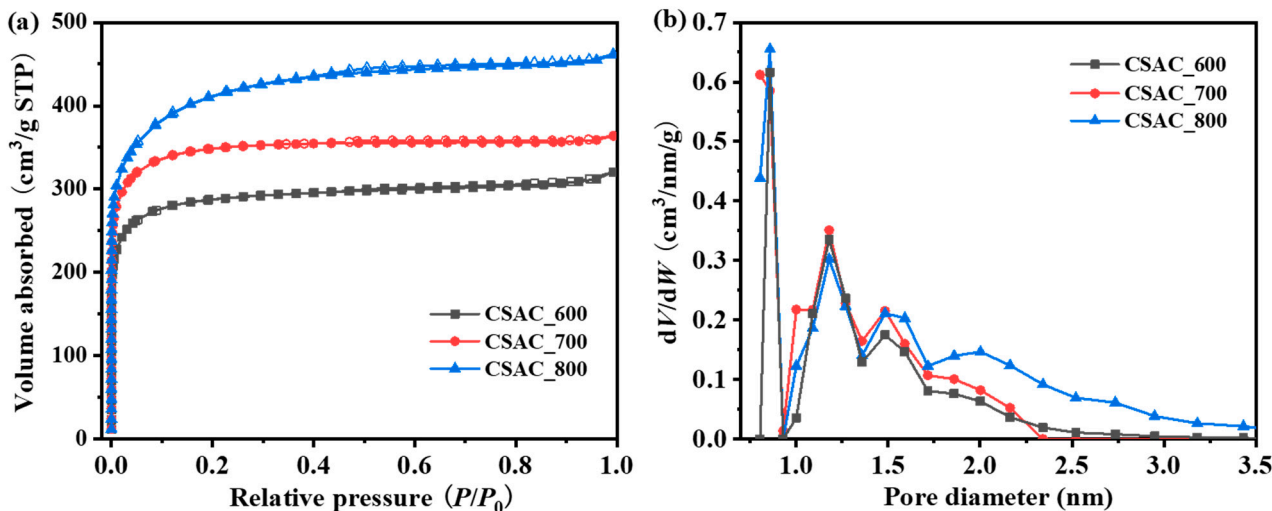

Figure 2. (**a**) N_2 adsorption-desorption isotherm and (**b**) pore size distribution of three coconut shell-activated carbons.

Table 2. Elemental analysis results for coconut shell activated carbon.

Samples	C (%)	H (%)	O (%)
CSAC_600	73.83	1.21	24.96
CSAC_700	77.59	1.00	21.41
CSAC_800	84.75	0.26	14.99

3.2. Adsorption Kinetics

The adsorption kinetics of F-53B by three coconut shell activated carbons were investigated in this study, and the results are shown in Figure 3a. At the first 20 min, F-53B was quickly adsorbed to coconut shell activated carbon, which can be attributed to the large number of adsorption sites on the coconut shell activated carbons. Due to the long hydrophobic C-F chains in F-53B (Figure 1) and the hydrophobicity of activated carbon, the hydrophobic interaction contributed to the quick adsorption of F-53B onto coconut shell activated carbon [38]. In addition, π-π interaction also contributes to the adsorption of F-53B onto coconut shell activated carbon [39,40]. With the progress of adsorption, the adsorption sites were gradually occupied by F-53B molecules, and the density of exposed adsorption sites decreased. Therefore, the concentration difference between the F-53B molecules adsorbed on the surface of coconut shell activated carbon and the F-53B molecules in solution decreased, the driving force for F-53B diffusion weakened, and the adsorption rate slowed down. After reactions for 60, 180, and 420 min, the adsorption of F-53B on CSAC800, CSAC_700, and CSAC-600 was closed to equilibrium, respectively. CSAC_800 has a higher adsorption rate for F-53B, which may be due to the larger specific surface area and pore volume of CSAC_800 than that of CSAC_600 and CSAC_700 (Table 1). After reactions for 24 h, the adsorption capacity of CSAC_800 and CSAC_700 for F-53B was approximately the same, and the removal rate of F-53B was about 100%, both higher than that of CSAC_600 (87.7%) (Figure 3b). This was attributed to the excess adsorption sites of CSAC_800 and CSAC_700 at the initial concentration of 0.2 g/L for 50 mg/L F-53B, and the CSAC_800 and CSAC_700 did not reach adsorption saturation when F-53B in the system was completely adsorbed. However, the lower specific surface area and small number of adsorption sites of CSAC_600 resulted in its lower adsorption capacity for F-53B.
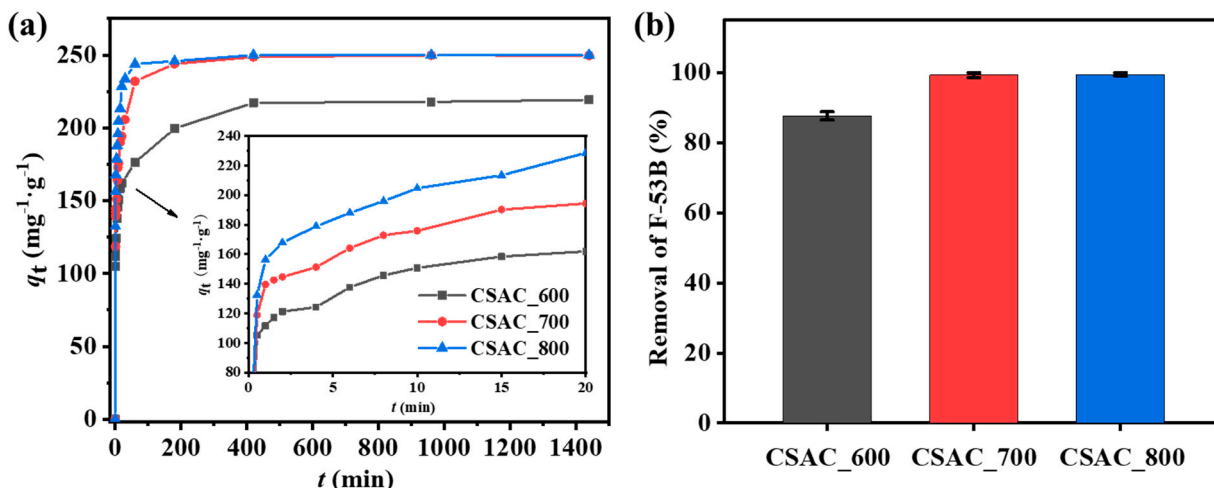
Figure 3. (**a**) Adsorption kinetic curves of F-53B at 25 °C and pH 7.0, (**b**) the removal rate of F-53B after reactions for 24 h.

The adsorption kinetics of F-53B were further analyzed using pseudo-first-order and pseudo-second-order kinetic models (Figure 4 and Table 3). The fitting results showed that the experimental data were better fitted by the pseudo-second-order kinetic model than that by the pseudo-first-order kinetic models, along with much higher correlation coefficient values ($R^2 \geq 0.9999$) (Table 3), indicating that the adsorption of F-53B involved chemical reactions rather than only physical diffusion [41].
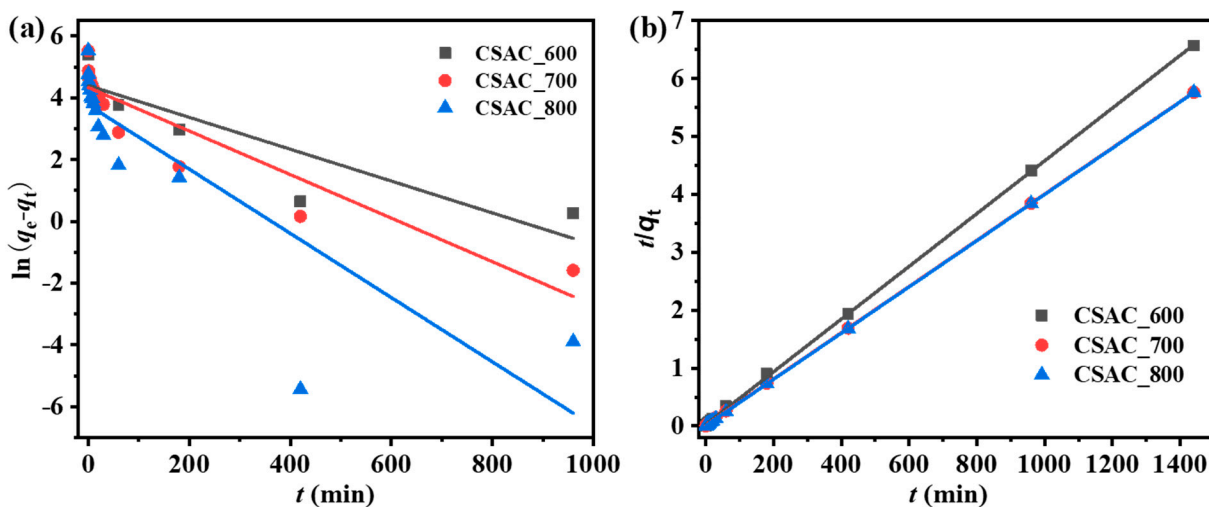

Figure 4. The adsorption kinetics of F-53B are fitted by (**a**) a pseudo-first-order model and (**b**) a pseudo-second-order model.

Table 3. Kinetic parameters of pseudo-first-order and pseudo-second-order models.

Kinetic Models	Kinetic Parameters	CSAC_600	CSAC_700	CSAC_800
Pseudo-first-order	$q_e/(\text{mg·g}^{-1})$	81.43	76.38	43.36
	$k_1/(\text{min}^{-1})$	0.005	0.007	0.010
	R^2	0.8222	0.8573	0.7119
Pseudo-second-order	$q_e/(\text{mg·g}^{-1})$	219.30	250.63	250.63
	$k_2/(\text{g·mg}^{-1}\text{·min}^{-1})$	8.6×10^{-4}	1.19×10^{-3}	2.4×10^{-3}
	R^2	0.9999	0.9999	0.9999

3.3. Adsorption Isotherm

Figure 5 exhibits the adsorption isotherms of F-53B by three coconut shell-activated carbons. The adsorption capacities of coconut shell activated carbons for F-53B increased quickly at low concentrations (<10 mg/L) and then increased slowly to equilibrium at high concentrations (>10 mg/L). The rapid adsorption performance at low concentrations indicated that the coconut shell activated carbons were very effective in removing F-53B from wastewater. As shown in Figure 5, CSAC_800 has the highest adsorption capacity for F-53B, followed by CSAC_700 and CSAC_600, which may be attributed to the fact that CSAC_800 has a larger specific surface area and a larger number of adsorption sites than that of CSAC_700 and CSAC_600.
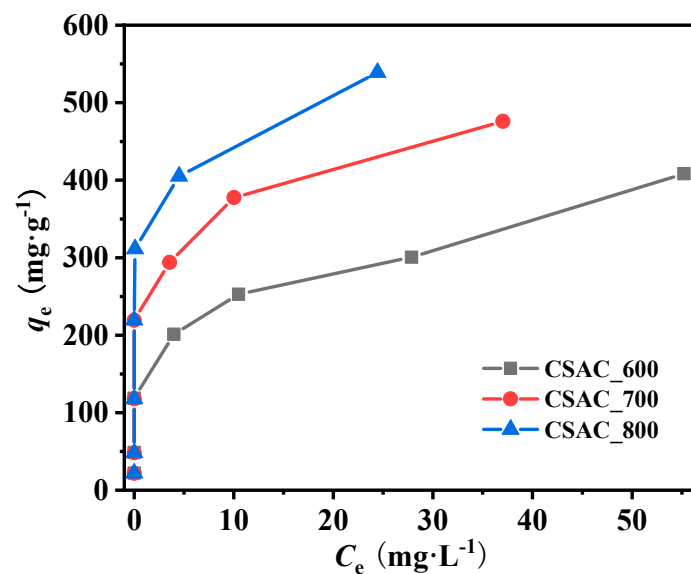

Figure 5. Adsorption isotherms of F-53B on CSAC adsorbents at 25 °C.

The adsorption isotherm of F-53B was further analyzed using the Langmuir and Freundlich models. As shown in Figure 6, the Langmuir model is described much better than the Freundlich model, with a higher R^2 for the Langmuir model ($\geq$0.9664) than that for the Freundlich model ($\leq$0.8733) (Table 4), indicating that the adsorption of F-53B on coconut shell activated carbons was mainly monolayer adsorption [42]. According to the fitting results of Langmuir models, the maximum adsorption capacities of CSAC_800, CSAC_700, and CSAC_600 were 537.63 mg/g, 476.19 mg/g, and 396.83 mg/g, respectively, being consistent with the experimental results (Figure 5) that CSAC_800 has a higher adsorption capacity for F-53B than CSAC_700 and CSAC_600. Compared with previous studies (Table 5) [23,43,44], the adsorption capacity of coconut shell activated carbons for F-53B was higher than that of alumina nanopowder, alumina nanowires, hydrophilic bentonite nanoclay, and surface modified nanoclay, but lower than that of anion-exchange resin IRA67 and layered double hydroxides. Given that the actual wastewater contains other pollutants (such as heavy metals), the adsorption capacity of coconut shell activated carbons for F-53B may be reduced when treating the actual wastewater, which needs further investigation.

Table 4. Adsorption isotherm parameters of the Langmuir and Freundlich models.

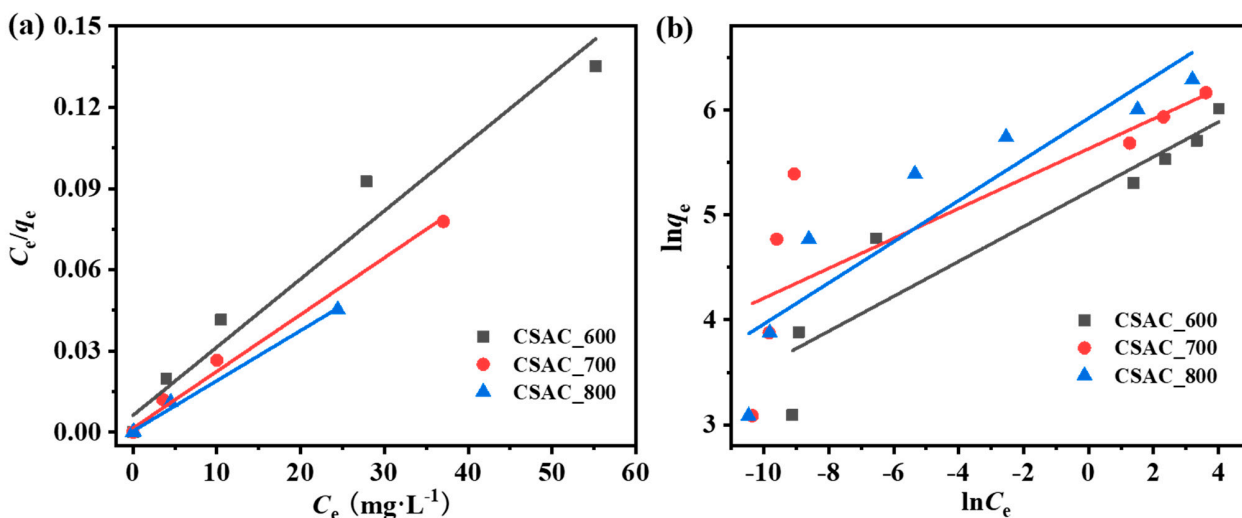| Isotherm Models	Isotherm Parameters	CSAC_600	CSAC_700	CSAC_800
Langmuir	$q_m/(\text{mg·g}^{-1})$	396.83	476.19	537.63
	$K_L/(\text{L·mg}^{-1})$	0.41	1.44	4.56
	R^2	0.9664	0.9923	0.9963
Freundlich	n	6.02	7.01	5.10
	$K_F/(\text{mg·g}^{-1})·(\text{L·mg}^{-1})^{1/n}$	185.22	278.98	372.97
	R^2	0.8733	0.6619	0.8329

Figure 6. Adsorption isotherms are fitted by (**a**) the Langmuir model and (**b**) the Freundlich model.

Table 5. Adsorption capacity of some adsorbents for F-53B.

Adsorbents	Adsorption Capacity (mg·g^{-1})	Reference
CSAC_600	396.83	This work
CSAC_700	476.19	This work
CSAC_800	537.63	This work
Alumina nanopowder	0.87	[43]
Alumina nanowires	0.09	[43]
Hydrophilic bentonite nanoclay	0.01	[43]
Surface modified nanoclay	2.47	[43]
Anion-exchange resin IRA67	2232.3	[23]
Layered double hydroxides	>860	[44]

3.4. Theoretical Calculations

The nanopores of coconut shell-activated carbons provide a good place for the adsorption of F-53B. To investigate the adsorption of F-53B on coconut shell activated carbons with different pore sizes, the adsorption energy was calculated. Since the pore sizes of these three materials are mainly distributed at 0.8 nm, 12 nm, and 1.5 nm, the adsorption energy of F-53B on coconut shell activated carbons with these three pore sizes was calculated in this study. As shown in Figure 7a, under the condition of a 0.8 nm pore size, the adsorption energies of F-53B on CSAC_600, CSAC_700, and CSAC_800 were -52.8 kcal/mol, -52.6 kcal/mol, and -46.7 kcal/mol, respectively, indicating that the adsorption energy of F-53B on CSAC_800 was lower than that of CSAC_600 and CSAC_700. Moreover, under the conditions of 1.2 nm and 1.5 nm pore sizes, the CSAC_800 also had a lower adsorption energy for F-53B than the CSAC_600 and CSAC_700 (Figure 7b,c). The lower adsorption energy is favorable for the adsorption of F-53B onto coconut shell activated carbons; thus, the results (Figure 7) of this work indicate that F-53B is transported more easily in CSAC_800 than in CSAC_600 and CSAC_700 at all pore sizes studied. Due to the high content of oxygen in CSAC_600 (Table 2), its degree of defect is large, which resulted in the adsorption energy between F-53B and different sites on CSAC_600 varying greatly. Therefore, when the pore size increased to 1.2 nm and 1.5 nm, the adsorption energy curves of F-53B on CSAC_600 showed two different peaks (Figure 7b,c). Table 6 exhibits the self-diffusion coefficients of F-53B molecules in CSAC absorbents with different pore sizes. It can be found that CSAC_800 had the highest self-diffusion coefficients under all studied pore sizes, which was attributed to the lowest adsorption energy of F-53B on CSAC_800 (Figure 7). Furthermore, CSAC_800 had the highest self-diffusion coefficients, which was one of the reasons why CSAC_800 had a higher adsorption rate for F-53B than CSAC_600 and CSAC_700 (Figure 3a).
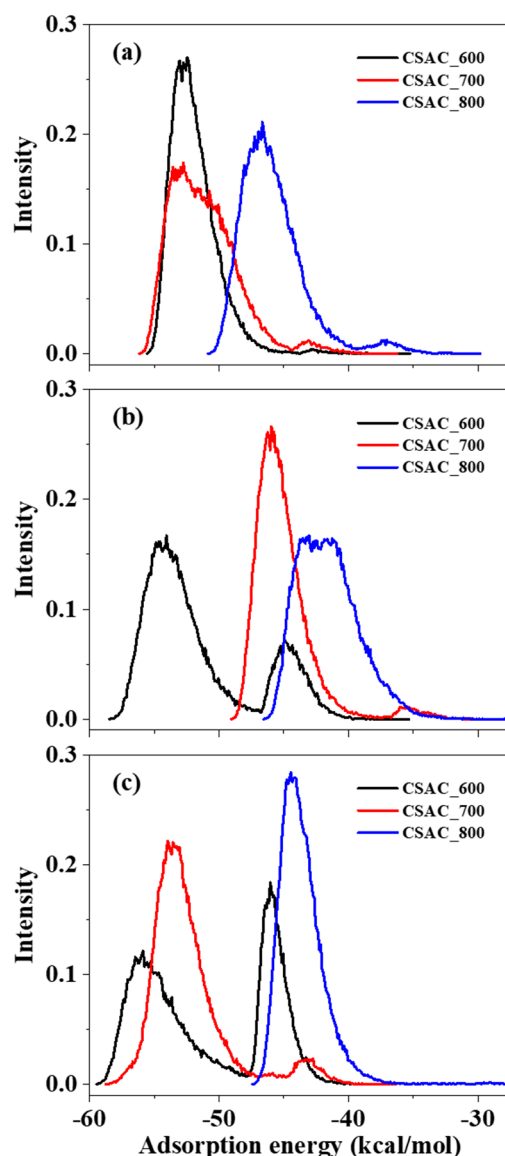
Figure 7. Adsorption energy distribution of F-53B on three coconut shell activated carbons with pore sizes of (**a**) 0.8 nm, (**b**) 1.2 nm, and (**c**) 1.5 nm.

Table 6. The self-diffusion coefficients of F-53B on three coconut shell- activated carbons with different pore sizes.

Pore Sizes	CSAC_600	CSAC_700	CSAC_800
0.8 nm	7.08	10.07	9.82
1.2 nm	9.20	9.38	8.90
1.5 nm	13.92	14.50	13.70

To investigate the interaction between F-53B and CSAC_800, the RDF curves between different atoms in F-53B and different adsorption sites on CSAC_800 are analyzed in this study. As shown in Figure 8a, the shortest distance between F/Cl atoms in F-53 B molecules and C atoms in CSAC_800 is more than 5 Å, while the shortest distance between O atoms in F-53 B molecules and C atoms in CSAC_800 is 4.6 Å. In addition, the shortest distance between F/Cl/O atoms in F-53 B molecules and O atoms in CSAC_800 is more than 5 Å (Figure 8b). As shown in Figure 8c, the shortest distance between F-53B molecule and H atoms in CSAC_800 is significantly smaller than that between F-53B molecule and other atoms in CSAC_800, and the shortest distance between F, Cl, and O atoms in F-53B and

H atoms in CSAC_800 is 3.67 Å, 2.85 Å, and 2.47 Å, respectively. This indicated that the interaction between the F-53B molecule and CSAC_800 was dominated by the interaction between F, Cl, and O atoms in F-53B and H atoms in CSAC_800, where the interaction between O atoms in F-53B and H atoms in CSAC_800 was the most important.
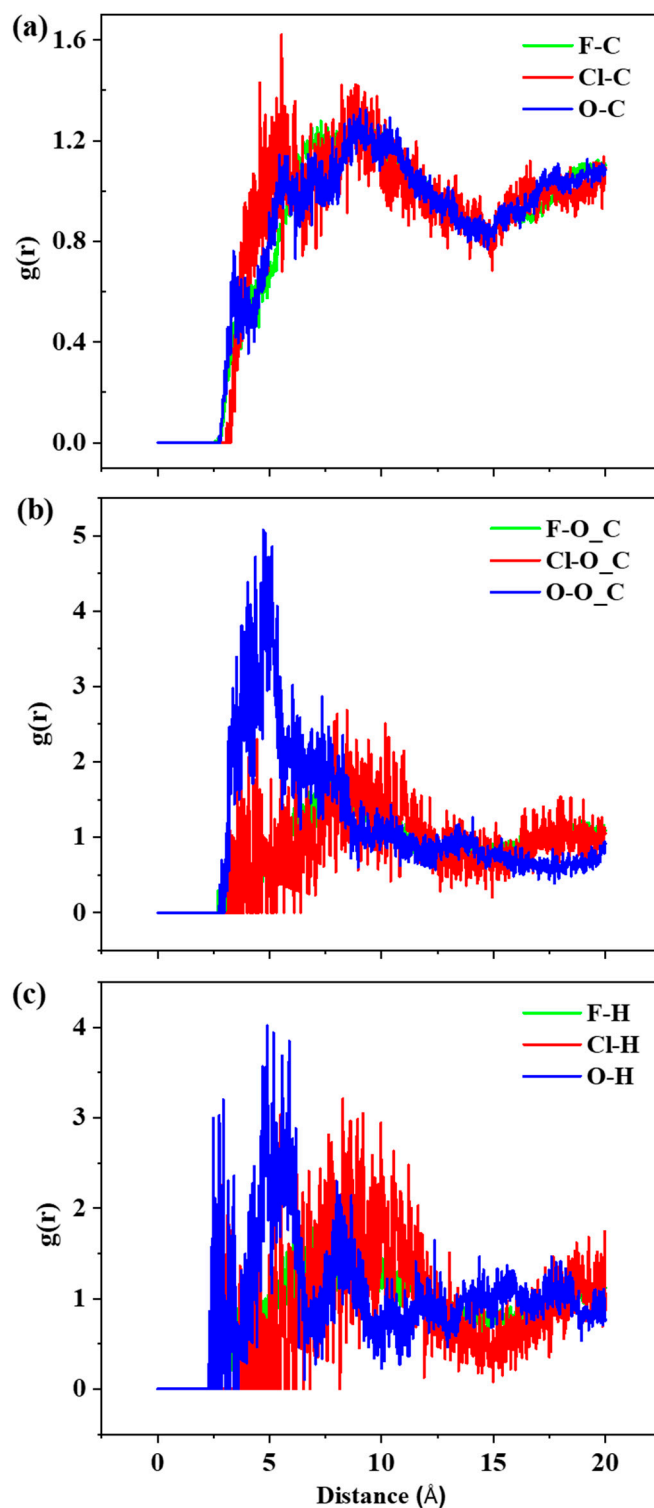

Figure 8. RDF curves between different atoms in F-53B and elements (**a**) C, (**b**) O, and (**c**) H in CSAC_800.

4. Conclusions

In this study, three coconut shell-active carbons were successfully synthesized via a simple one-step KOH activation method. The coconut shell activated carbon synthesized at 800 °C (CSAC_800) had a more developed nanopore structure than that synthesized at 600 °C (CSAC_600) and 700 °C (CSAC_700), which is favorable for the adsorption of F-53B. Adsorption experiments showed that the adsorption of F-53B on coconut shell active carbons followed the Langmuir isotherm model and pseudo-second-order kinetic model. The maximum adsorption capacity of CSAC_800 for F-53B was 537.63 mg/g, higher than that of CSAC_600 (396.83 mg/g) and CSAC_700 (476.19 mg/g), which was attributed to the higher specific surface area and larger number of adsorption sites of CSAC_800 for F-53B. The adsorption rate of CSAC_800 was also higher than that of CSAC_600 and CSAC_700, which was attributed to the lower adsorption energy and higher self-diffusion coefficients of CSAC_800 for F-53B. Considering the low cost and high performance of coconut shell activated carbon, it is expected to add an adsorption process before the coagulation treatment of electroplating wastewater to improve the removal efficiency of F-53B. Overall, the results of this study indicated that the adsorptive removal of F-53B by CSAC_800 has a good application prospect.

Author Contributions: Conceptualization, H.Y.; Data curation, H.Y., X.C. and Z.L.; Formal analysis, H.X., K.C. and Y.H.; Investigation, H.Y., X.C. and Z.L.; Methodology, H.Y., X.C. and Z.L.; Writing—original draft, H.Y., X.C. and Z.L.; Writing—review and editing, H.X., Z.D., K.C. and Y.H. All authors have read and agreed to the published version of the manuscript.

Data Availability Statement: The data presented in this study are available on request from the corresponding author.

Conflicts of Interest: The authors declare that they have no known competing financial interests or personal relationships that could have appeared to influence the work reported in this paper.

Nomenclature

F-53B	chlorinated polyfluoroalkyl ether sulfonates
CSAC_600	coconut shell activated carbon prepared at 600 °C
CSAC_700	coconut shell activated carbon prepared at 700 °C
CSAC_800	coconut shell activated carbon prepared at 800 °C
q_t	adsorption capacities at time t
q_e	adsorption capacities at equilibrium
q_m	the maximum adsorption capacity
C_0	concentrations of F-53B at the adsorption times at zero
C_t	concentrations of F-53B at the adsorption times at t
C_e	concentrations of F-53B at the adsorption times at equilibrium

References

1. Hu, Y.; Guo, M.; Zhang, S.; Jiang, W.; Xiu, T.; Yang, S.; Kang, M.; Dongye, Z.; Li, Z.; Wang, L. Microwave synthesis of metal-organic frameworks absorbents (DUT-5-2) for the removal of PFOS and PFOA from aqueous solutions. *Microporous Mesoporous Mater.* **2022**, *333*, 111740. [CrossRef]
2. Leung, S.C.E.; Shukla, P.; Chen, D.; Eftekhari, E.; An, H.; Zare, F.; Ghasemi, N.; Zhang, D.; Nguyen, N.-T.; Li, Q. Emerging technologies for PFOS/PFOA degradation and removal: A review. *Sci. Total Environ.* **2022**, *827*, 153669. [CrossRef] [PubMed]
3. Zhang, R.; Hu, Z.; Wei, H.; Zhang, S.; Meng, X. Adsorption of perfluorooctane sulfonate on carbonized poly-melamine-formaldehyde sponge. *Sci. Total Environ.* **2020**, *727*, 138626. [CrossRef] [PubMed]
4. Jane, L.; Espartero, L.; Yamada, M.; Ford, J.; Owens, G.; Prow, T.; Juhasz, A. Health-related toxicity of emerging per- and polyfluoroalkyl substances: Comparison to legacy PFOS and PFOA. *Environ. Res.* **2022**, *212*, 113431. [CrossRef] [PubMed]
5. Lu, Y.; Liang, Y.; Zhou, Z.; Wang, Y.; Jiang, G. Possible fluorinated alternatives of PFOS and PFOA: Ready to go? *Environ. Sci. Technol.* **2019**, *53*, 14091–14092. [CrossRef]

6. Wang, Q.; Huang, J.; Liu, S.; Wang, C.; Jin, Y.; Lai, H.; Tu, W. Aberrant hepatic lipid metabolism associated with gut microbiota dysbiosis triggers hepatotoxicity of novel PFOS alternatives in adult zebrafish. *Environ. Int.* **2022**, *166*, 107351. [CrossRef]

7. Wang, S.; Huang, J.; Yang, Y.; Hui, Y.; Ge, Y.; Larssen, T.; Yu, G.; Deng, S.; Wang, B.; Harman, C. First report of a Chinese PFOS alternative overlooked for 30 years: Its toxicity, persistence, and presence in the environment. *Environ. Sci. Technol.* **2013**, *47*, 10163–10170. [CrossRef]

8. Liu, S.; Lai, H.; Wang, Q.; Martínez, R.; Zhang, M.; Liu, Y.; Huang, J.; Deng, M.; Tu, W. Immunotoxicity of F53B, an alternative to PFOS, on zebrafish (Danio rerio) at different early life stages. *Sci. Total Environ.* **2021**, *790*, 148165. [CrossRef]

9. He, Y.; Lv, D.; Li, C.; Liu, X.; Liu, W.; Han, W. Human exposure to F-53B in China and the evaluation of its potential toxicity: An overview. *Environ. Int.* **2022**, *161*, 107108. [CrossRef]

10. Militao, I.M.; Roddick, F.A.; Bergamasco, R.; Fan, L. Removing PFAS from aquatic systems using natural and renewable material-based adsorbents: A review. *J. Environ. Chem. Eng.* **2021**, *9*, 105271. [CrossRef]

11. Saeidi, N.; Kopinke, F.-D.; Georgi, A. What is specific in adsorption of perfluoroalkyl acids on carbon materials? *Chemosphere* **2021**, *273*, 128520. [CrossRef] [PubMed]

12. Mohd Azmi, L.H.; Williams, D.R.; Ladewig, B.P. Polymer-assisted modification of metal-organic framework MIL-96 (Al): Influence of HPAM concentration on particle size, crystal morphology and removal of harmful environmental pollutant PFOA. *Chemosphere* **2021**, *262*, 128072. [CrossRef]

13. Albert, K.; Hsieh, P.-Y.; Chen, T.-H.; Hou, C.-H.; Hsu, H.-Y. Diatom-assisted biomicroreactor targeting the complete removal of perfluorinated compounds. *J. Hazard. Mater.* **2020**, *384*, 121491. [CrossRef] [PubMed]

14. D'Agostino, L.A.; Mabury, S.A. Aerobic biodegradation of 2 fluorotelomer sulfonamide–based aqueous film–forming foam components produces perfluoroalkyl carboxylates. *Environ. Toxicol. Chem.* **2017**, *36*, 2012–2021. [CrossRef] [PubMed]

15. Wu, Y.; Hu, Y.; Han, M.; Ouyang, Y.; Xia, L.; Huang, X.; Hu, Z.; Li, C. Mechanism insights into the facet-dependent photocatalytic degradation of perfluorooctanoic acid on BiOCl nanosheets. *Chem. Eng. J.* **2021**, *425*, 130672. [CrossRef]

16. Liu, F.; Guan, X.; Xiao, F. Photodegradation of per- and polyfluoroalkyl substances in water: A review of fundamentals and applications. *J. Hazard. Mater.* **2022**, *439*, 129580. [CrossRef]

17. Wen, Y.; Rentería-Gómez, Á.; Day, G.S.; Smith, M.F.; Yan, T.-H.; Ozdemir, R.O.K.; Gutierrez, O.; Sharma, V.K.; Ma, X.; Zhou, H.-C. Integrated photocatalytic reduction and oxidation of perfluorooctanoic acid by metal–organic frameworks: Key insights into the degradation mechanisms. *J. Am. Chem. Soc.* **2022**, *144*, 11840–11850. [CrossRef]

18. Duan, X.; Wang, W.; Wang, Q.; Sui, X.; Li, N.; Chang, L. Electrocatalytic degradation of perfluoroocatane sulfonate (PFOS) on a 3D graphene-lead dioxide (3DG-PbO$_2$) composite anode: Electrode characterization, degradation mechanism and toxicity. *Chemosphere* **2020**, *260*, 127587. [CrossRef]

19. Soriano, A.; Schaefer, C.; Urtiaga, A. Enhanced treatment of perfluoroalkyl acids in groundwater by membrane separation and electrochemical oxidation. *Chem. Eng. J. Adv.* **2020**, *4*, 100042. [CrossRef]

20. Pierpaoli, M.; Szopińska, M.; Wilk, B.K.; Sobaszek, M.; Łuczkiewicz, A.; Bogdanowicz, R.; Fudala-Książek, S. Electrochemical oxidation of PFOA and PFOS in landfill leachates at low and highly boron-doped diamond electrodes. *J. Hazard. Mater.* **2021**, *403*, 123606. [CrossRef]

21. Pauletto, P.S.; Bandosz, T.J. Activated carbon versus metal-organic frameworks: A review of their PFAS adsorption performance. *J. Hazard. Mater.* **2022**, *425*, 127810. [CrossRef]

22. Uddin, M.K. A review on the adsorption of heavy metals by clay minerals, with special focus on the past decade. *Chem. Eng. J.* **2017**, *308*, 438–462. [CrossRef]

23. Gao, Y.; Deng, S.; Du, Z.; Liu, K.; Yu, G. Adsorptive removal of emerging polyfluoroalky substances F-53B and PFOS by anion-exchange resin: A comparative study. *J. Hazard. Mater.* **2017**, *323*, 550–557. [CrossRef] [PubMed]

24. Hassan, M.; Liu, Y.; Naidu, R.; Du, J.; Qi, F. Adsorption of perfluorooctane sulfonate (PFOS) onto metal oxides modified biochar. *Environ. Technol. Innov.* **2020**, *19*, 100816. [CrossRef]

25. Liu, K.; Zhang, S.; Hu, X.; Zhang, K.; Roy, A.; Yu, G. Understanding the adsorption of PFOA on MIL-101(Cr)-based anionic-exchange metal–organic frameworks: Comparing DFT calculations with aqueous sorption experiments. *Environ. Sci. Technol.* **2015**, *49*, 8657–8665. [CrossRef]

26. Park, M.; Wu, S.; Lopez, I.J.; Chang, J.Y.; Karanfil, T.; Snyder, S.A. Adsorption of perfluoroalkyl substances (PFAS) in groundwater by granular activated carbons: Roles of hydrophobicity of PFAS and carbon characteristics. *Water Res.* **2020**, *170*, 115364. [CrossRef]

27. Barker, J.A.; Henderson, D. What is "liquid"? Understanding the states of matter. *Rev. Modern Phys.* **1976**, *48*, 587–671. [CrossRef]

28. Rappe, A.K.; Casewit, C.J.; Colwell, K.S.; Goddard, W.A., III; Skiff, W.M. UFF, a full periodic table force field for molecular mechanics and molecular dynamics simulations. *J. Am. Chem. Soc.* **1992**, *114*, 10024–10035. [CrossRef]

29. Ekramipooya, A.; Valadi, F.M.; Latifi Pour, M.; Rashtchian, D.; Gholami, M.R. Effect of the pyrrolic nitrogen functional group in the selective adsorption of CO$_2$: GCMC, MD, and DFT studies. *Energy Fuels* **2021**, *35*, 15918–15934. [CrossRef]

30. Long, H.; Lin, H.-F.; Yan, M.; Bai, Y.; Tong, X.; Kong, X.-G.; Li, S.-G. Adsorption and diffusion characteristics of CH$_4$, CO$_2$, and N$_2$ in micropores and mesopores of bituminous coal: Molecular dynamics. *Fuel* **2021**, *292*, 120268. [CrossRef]

31. Ning, H.; Yang, Z.; Yin, Z.; Wang, D.; Meng, Z.; Wang, C.; Zhang, Y.; Chen, Z. A novel strategy to enhance the performance of CO$_2$ adsorption separation: Grafting hyper-cross-linked polyimide onto composites of UiO-66-NH$_2$ and GO. *ACS Appl. Mater. Interfaces* **2021**, *13*, 17781–17790. [CrossRef] [PubMed]

32. Cheng, Z.; Shang, C.; Westerhoff, P.; Ling, L. Novel polymer optical fibers with high mass-loading g-C$_3$N$_4$ embedded metamaterial porous structures achieve rapid micropollutant degradation in water. *Water Res.* **2023**, *242*, 120234. [CrossRef]

33. Hidayu, A.R.; Mohamad, N.F.; Matali, S.; Sharifah, A.S.A.K. Characterization of activated carbon prepared from oil palm empty fruit bunch using BET and FT-IR techniques. *Procedia Eng.* **2013**, *68*, 379–384. [CrossRef]

34. Saka, C. BET, TG–DTG, FT-IR, SEM, iodine number analysis and preparation of activated carbon from acorn shell by chemical activation with ZnCl$_2$. *J. Anal. Appl. Pyrolysis* **2012**, *95*, 21–24. [CrossRef]

35. Lua, A.C.; Yang, T. Effect of activation temperature on the textural and chemical properties of potassium hydroxide activated carbon prepared from pistachio-nut shell. *J. Colloid Interface Sci.* **2004**, *274*, 594–601. [CrossRef] [PubMed]

36. Tseng, R.L.; Tseng, S.K.; Wu, F.C.; Hu, C.C.; Wang, C.C. Effects of micropore development on the physicochemical properties of KOH-activated carbons. *J. Chin. Inst. Chem. Eng.* **2008**, *39*, 37–47. [CrossRef]

37. Romanos, J.; Beckner, M.; Rash, T.; Firlej, L.; Kuchta, B.; Yu, P.; Suppes, G.; Wexler, C.; Pfeifer, P. Nanospace engineering of KOH activated carbon. *Nanotechnology* **2012**, *23*, 015401. [CrossRef]

38. Yu, Q.; Zhang, R.; Deng, S.; Huang, J.; Yu, G. Sorption of perfluorooctane sulfonate and perfluorooctanoate on activated carbons and resin: Kinetic and isotherm study. *Water Res.* **2009**, *43*, 1150–1158. [CrossRef]

39. Dai, Y.; Zhao, J.; Sun, C.; Li, D.; Liu, X.; Wang, Z.; Yue, T.; Xing, B. Interaction and combined toxicity of microplastics and perand polyfluoroalkyl substances in aquatic environment. *Front. Environ. Sci. Eng.* **2022**, *16*, 136. [CrossRef]

40. Wang, W.; Mi, X.; Shi, H.; Zhang, X.; Zhou, Z.; Li, C.; Zhu, D. Adsorption behaviour and mechanism of the PFOS substitute OBS (sodium p-perfluorous nonenoxybenzene sulfonate) on activated carbon. *R. Soc. Open Sci.* **2019**, *6*, 191069. [CrossRef]

41. Gong, Y.; Wang, L.; Liu, J.; Tang, J.; Zhao, D. Removal of aqueous perfluorooctanoic acid (PFOA) using starch-stabilized magnetite nanoparticles. *Sci. Total Environ.* **2016**, *562*, 191–200. [CrossRef] [PubMed]

42. Xu, J.; Liu, Z.; Zhao, D.; Gao, N.; Fu, X. Enhanced adsorption of perfluorooctanoic acid (PFOA) from water by granular activated carbon supported magnetite nanoparticles. *Sci. Total Environ.* **2020**, *723*, 137757. [CrossRef] [PubMed]

43. Zhao, S.; Liu, S.; Wang, F.; Lu, X.; Li, Z. Sorption behavior of 6:2 chlorinated polyfluorinated ether sulfonate (F-53B) on four kinds of nano-materials. *Sci. Total Environ.* **2021**, *757*, 144064. [CrossRef] [PubMed]

44. Ding, D.; Song, X.; Wei, C.; Hu, Z.; Liu, Z. Efficient sorptive removal of F-53B from water by layered double hydroxides: Performance and mechanisms. *Chemosphere* **2020**, *252*, 126443. [CrossRef] [PubMed]